Dynamic Pattern Formation of Microparticles in a Uniform Flow by an On-Chip Thermophoretic Separation Device

Tetsuro Tsuji,[*] Sho Saita, and Satoyuki Kawano[†]

Graduate School of Engineering Science, Osaka University, 1-3 Machikaneyama, Toyonaka, Osaka 560-8531, Japan

(Received 8 October 2017; revised manuscript received 22 January 2018; published 28 February 2018)

Thermophoresis is the motion of micro- or nanoparticles driven by the temperature gradient of the surrounding fluid. We develop an on-chip microfluidic device to induce the thermophoresis of microparticles. It is clarified that both the bulk material and the chemical modification to the surface affect the thermophoresis of particles in an aqueous solution, even regarding the direction of particle motion. Polystyrene (PS) beads with a diameter of 1 μm show a thermophobic response to a temperature gradient induced on the developed microfluidic device and move toward the colder region. The interplay between a uniform flow in the microchannel and thermophoresis leads to a dynamic pattern formation of the PS beads in the upstream region. Thus, a purified solution can be obtained in the downstream region, demonstrating the potential of thermophoresis as a microparticle filter. Furthermore, silica beads with a diameter of 1 μm move toward the hotter region on the device. Therefore, the PS and silica beads show the opposite response to the temperature gradient despite having the same diameter and surface modification. The thermophoretic separation of a mixture of the PS and silica beads is demonstrated.

DOI: 10.1103/PhysRevApplied.9.024035

I. INTRODUCTION

The temperature gradient in fluids induces the transport of micro- and nanoparticles. This phenomenon, called thermophoresis [1–3], has drawn attention for its potential use in controlling target objects without using electrical or optical forces, which are frequently used in technology to manipulate micro- or nanoscale objects. Although there are a number of ongoing theoretical [4–7] and numerical [8–11] studies designed to understand the nature of thermophoresis, experimental studies seem to be more prevalent. In fact, recent developments in experimental thermophoretic techniques have provided alternative methods of assembling colloids [12], increasing the concentration of DNA [13], measuring protein bindings [14–16], and detecting differences in the conformation of DNA [17,18]. The thermophoresis of biomolecules [19,20], colloids [21–28], and micron-sized objects such as cells [29] has also been investigated systematically, and the range of thermophoresis applications is growing. For example, the thermophoretic manipulation of biomolecules through nanopore sensors in nano- and microfluidic devices was proposed and numerically simulated by He *et al.* [30]. The selective thermophoretic manipulation of cells or biomolecules to desired locations in on-chip devices [31–34] is expected to enhance the efficiency and accuracy of sensing by increasing the concentration of targets near sensor sites.

However, the bottleneck in the development of manipulation technologies using thermophoresis is that it is a rather weak phenomenon. More specifically, thermophoresis is easily obscured by other effects, such as the convection of the surrounding fluid, the diffusion of target objects, and optical and electrical forces. To integrate micro- and nanoparticle thermophoresis into manipulation technologies, one would need a device that can create a large temperature gradient on the order of 100 K mm^{-1} to overcome these other effects. At the same time, thermal convection must be suppressed. Such a situation is unachievable for millimeter-scale aqueous solutions. Thermophoresis experiments with weaker temperature gradients are also possible if they are conducted over tens of minutes (or several hours) until the concentration gradient produced by thermophoresis becomes detectable [24,35–37]. When considering the application of thermophoresis to nano- and microfluidic devices, faster responses are preferable for a higher feasibility.

To create a large temperature gradient, irradiation by laser (see, e.g., Refs. [13,14,18,19,38–40]) is often attractive because it enables the noncontact and highly localized heating of fluids with a length scale of tens of micrometers. However, fluid channel heights are sometimes too large to suppress thermal convection, the fluid and temperature fields can be spatially two or three dimensional, and the optical effect should be carefully removed to discuss

[*]tsuji@me.es.osaka-u.ac.jp
[†]kawano@me.es.osaka-u.ac.jp

thermophoresis. The aim of this paper is to achieve thermophoresis in a microfluidic device with the thermophoresis overcoming the effects of thermal convection. A large temperature gradient is produced using microelectromechanical systems (MEMS) produced by microfabrication.

Previous papers have reported temperature control using Joule heat generated by conductive materials integrated into microfluidic devices [24,41–44]. In this paper, a microfluidic device with a thin-film electrode at the bottom of the fluid channel is fabricated. The electrode has a narrow line pattern, which enables local heating and thus the formation of a large temperature gradient. Thanks to the small scale of the geometry, the unwanted nonuniformities in the fluid and temperature fields are insignificant. The thermophoresis of microparticles is clearly observed at time scales on the order of tens of seconds and is characterized for particles composed of different bulk materials and with different chemically modified surfaces in aqueous solutions with and without a surfactant. In the developed microfluidic device, micron-sized polystyrene (PS) and silica particles show the opposite response to the temperature gradient. Dynamic pattern formation in the microfluidic device induced by the thermophoresis of the PS beads in a uniform flow is demonstrated. Finally, differences between the thermophoretic motions of the PS and silica beads are used to separate them in the microfluidic device.

II. EXPERIMENTAL DETAILS

A. Observation system

Figure 1 shows a schematic of the experimental setup. An inverted microscope (IX73, Olympus, Japan) with an objective lens (10 × magnification) is used to observe the experiments, and observed images are recorded using a CMOS camera (Zyla 5.5, Andor Technology, Northern Ireland), as shown in Fig. 1(a). The developed microfluidic device is mounted on the Al stage of the inverted microscope. The details of this device are described in Sec. II C. A mirror unit consisting of an excitation filter, a dichroic mirror, and an absorption filter is inserted into the microscope as shown in Fig. 1(a), and a mercury lamp (U-HGLGPS, Olympus, Japan) is used to induce the fluorescence of sample solutions. The details of the samples are described in Sec. II B. The mirror unit should be selected according to the wavelength of the fluorescence of the samples. An electric current I is applied to the thin-film Au electrode of the microfluidic device to generate Joule heat (see Sec. II C). The current I is regulated via a dc-stabilized power supply (PAN35-10A, Kikusui, Japan) controlled by a function generator (WF1973, NF Corporation, Japan). The function generator and the camera are synchronized. A sapphire plate, which has high thermal conductivity and optical transmissivity, is placed between the device and the Al stage to enhance the heat dissipation of the device. The stage is placed in a dark chamber to reduce background noise in the observation.

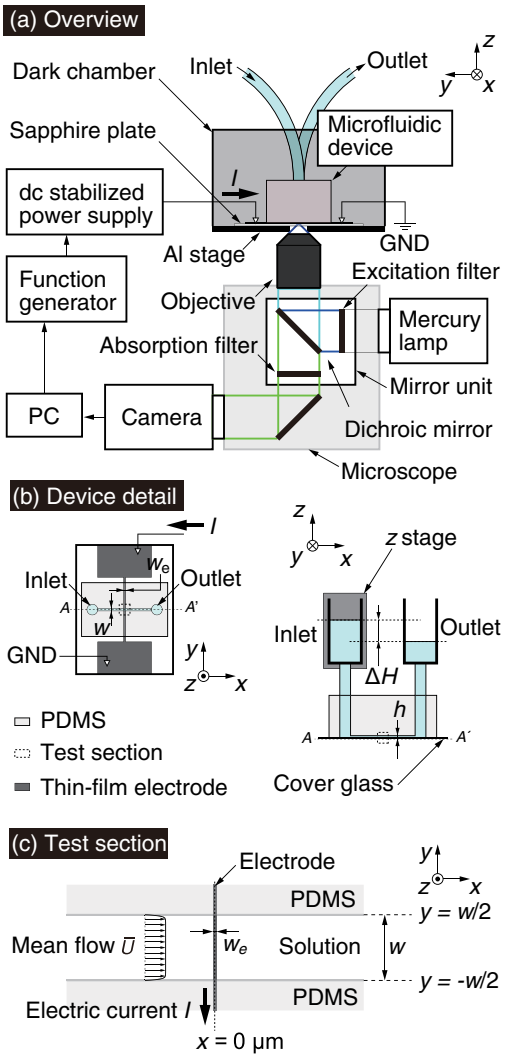

FIG. 1. (a) Overview of the experimental setup. An inverted microscope is used to observe the fluorescence of the sample solutions. An electric current I is applied to the electrode of the microfluidic device to induce Joule heating. (b) Details of the microfluidic device. (Left) Top view. (Right) Side view. The mean flow in the x direction is controlled by the water-level difference ΔH between the two reservoirs fixed to the z stage. (c) Schematic of the microscope view of the test section. GND: Ground and PC: Personal computer.

B. Microparticle characteristics

Table I lists the samples investigated in this paper. All samples are prepared in a tris(hydroxymethyl)aminomethane hydrochloride (tris-HCl) solution (pH = 8.0, Nippon Gene, Japan) with a concentration of 10 mM. To investigate the effect of the added surfactant, samples are also prepared by dispersion in a mixed solution of tris HCl (10 mM) and a surfactant (Triton X-100, 0.5 vol %, MP Biomedicals, Santa Ana, California). This surfactant is nonionic and is frequently used as a coating to chemically standardize the surfaces of beads [23,24].

TABLE I. List of samples investigated in this paper. The buffer solution tris HCl (10 mM) or a mixed solution of tris HCl (10 mM) and a nonionic surfactant (Triton X-100, 0.5 vol %) is used as the solvent. The microparticle diameter is 1 μm.

Case	Material	Surface modification	Surfactant	Remarks
1	PS	Carboxylate modified	No surfactant	PS 0.04 wt %
2	Silica	Carboxylate modified	No surfactant	Silica 0.1 wt %
3	Silica	No surface modification	No surfactant	Silica 0.1 wt %
4	PS	Carboxylate modified	With surfactant	PS 0.04 wt %
5	Silica	Carboxylate modified	With surfactant	Silica 0.1 wt %
6	Silica	No surface modification	With surfactant	Silica 0.1 wt %

The fluorescent molecule 2′, 7′-bis-(2-carboxyethyl)-5-(6)-carboxyfluorescein (BCECF, Molecular Probes, Eugene, Oregon) is used for the temperature measurement (Sec. III A). The fluorescence of BCECF is related to the pH of the solution, which is sensitive to the temperature of the tris-HCl buffer. Therefore, the addition of the tris HCl is necessary for the visualization of the temperature profile in the microchannel. The spatial temperature profile can be obtained by laser-induced fluorescence (LIF) [38,39].

PS (F8823, Molecular Probes, Eugene, Oregon) beads with a diameter of 1 μm are used in case 1. The surface of the PS beads is carboxylate modified, causing the surface to be negatively charged in a solution where $p\mathrm{H} = 8.0$.

Silica beads (40-02-103, sicastar®-redF, Micromod Partikeltechnologie, Germany) with the same diameter of 1 μm are used in case 2. The surface of the silica beads in case 2 is also carboxylate modified. The bulk characteristics of silica are different from those of PS in terms of thermal conductivity. The thermal conductivities of PS and silica are $\lambda_{\mathrm{PS}} \approx 0.15$ W m^{-1} K^{-1} [45,46] and $\lambda_{\mathrm{silica}} \approx 1.3$ W m^{-1} K^{-1} [47], respectively. The thermal conductivity of water is $\lambda_{\mathrm{water}} \approx 0.6$ W m^{-1} K^{-1}, which falls between λ_{PS} and $\lambda_{\mathrm{silica}}$.

Silica beads (42-00-103, sicastar-greenF, Micromod Partikeltechnologie, Germany) with no surface modification are used in case 3. A comparison between cases 2 and 3 thus shows the effect of the chemical modification of the surface. Cases 4, 5, and 6 are the same as cases 1, 2, and 3, respectively, but with the surfactant additive in the buffer solution.

C. Detail of microfluidic device

A top-down view of the microfluidic device is shown in the left side of Fig. 1(b). The microfluidic device consists of a glass substrate (18 × 24 mm) with a thickness of 0.2 mm and a polydimethylsiloxane (PDMS) block bonded to the substrate. A thin film of Au with a thickness of 150 nm is deposited onto the substrate, as indicated by the dark-gray region in Fig. 1(b). The Au thin film functions as a heater by inducing an electric current I. The width w_e of the electrode at the test section indicated by the dashed square in Fig. 1(b) is set to $w_e = 20$ μm. The PDMS block [the light-gray area in Fig. 1(b)] has a microchannel with a width of $w = 400$ μm and a height of $h = 17 \pm 0.2$ μm. The device dimensions are carefully designed to ensure that the thermophoresis can overcome the effects of thermal convection. Some details on the fabrication process are presented in the Appendix. Before the PDMS block and glass substrate are bonded, their contact surfaces are treated by oxygen plasma to enhance adhesion. The test section is defined as the intersection of the microchannel and the electrode [the left side of Fig. 1(b)]. The inlet and the outlet of the microchannel are connected to reservoirs, as shown in the side view of the device on the right side of Fig. 1(b). To remove the remaining bubbles and gases dissolved in the solution, the whole device is deaerated in a vacuum chamber.

Because of the small channel height ($h = 17$ μm) and the low numerical aperture (NA = 0.3) of the objective lens, the obtained images include the fluorescence of molecules or beads over the entire z dimension of the microchannel, from the lower to the upper surface [Fig. 1(c)]. Therefore, the results given in this paper represent information integrated over z. The small channel height, which is 17 times as large as the particle diameter, may cause the finite-size effect of particles. To avoid this effect, the volume fraction of the particles in the sample solution is less than 0.1% (see, Table I with the specific gravities of PS and silica, which are 1.05 and 2, respectively). On the other hand, the channel height is large enough to prevent the interaction between particles and confining surfaces from being significant.

The water-level difference ΔH of the reservoirs is controlled by an automatic stage (SGSP20-35, Sigma Koki, Japan) with a precision of 1 μm [right side of Fig. 1(b)]. The mean flow $\bar{U}$ in the x direction [Fig. 1(c)] is analyzed by particle image velocimetry (PIV). The flow field in a rectangular channel induced by the water-level difference ΔH can be explicitly obtained (see, e.g., Ref. [48]), and the flow is almost uniform in the y direction. To be more precise,

TABLE II. Mean flow velocity $\bar{U}$ in the microchannel investigated in this paper.

Solution	ΔH	Mean flow $\bar{U}$
Without surfactant	0 μm	0.01 ± 0.06 μm s^{-1}
	100 μm	4.6 ± 0.2 μm s^{-1}
With surfactant	0 μm	0.03 ± 0.03 μm s^{-1}
	100 μm	4.1 ± 0.1 μm s^{-1}

95% of the maximum flow speed is attained even near the PDMS wall; i.e., $|y| = 0.9(w/2)$. In this paper, the cases of $\Delta H = 0$ and 100 μm are investigated. The PIV results are summarized in Table II. Slight asymmetries with respect to the x direction, which will be addressed further in the discussion of Figs. 4 and 5, are attributable to the fluctuations in the mean velocity $\bar{U}$ shown in Table II.

III. RESULTS AND DISCUSSION

All experiments are conducted at room temperature ($T_0 = 295.5 \pm 0.3$ K. The resistance of the electrode is $R = 139 \pm 0.4\ \Omega$, and the electric current I is adjusted to achieve an electric power of $E = RI^2 = 0.34$ W. This value of E is smaller than $E_{\max} \approx 0.4$ W, at which the emergence of bubbles is observed. The electric current is applied at $t = 0$ s, and images are recorded with a camera for 300 s after this point. The center of the electrode is defined as $x = 0$ μm [Fig. 1(c)].

A. Temperature profile

This section presents the temperature measurement results using the BCECF solution. The temperature profiles obtained by LIF indicate that the temperature is uniform in the y direction [Fig. 1(c)]. Therefore, T is defined as the temperature averaged along the y direction, and T is plotted in Fig. 2 as a function of x. Here, the standard error over the y direction is 0.5 K at the most. The water-level difference is set to $\Delta H = 0$ μm, and the resulting mean flow is estimated as $|\bar{U}| < 0.1$ μm s^{-1} (Table II). As shown in Fig. 2, the temperature near the electrode increases over time. Consequently, the temperature away from the electrode also increases. To determine the time scale of the temporal development of the temperature field, $T_{\max} = \max_x(T)$ is plotted as a function of time, as shown in the inset of Fig. 2. Rapid changes in $T_{\max}$ occur for $t < 2$ s, and $T_{\max}$ slowly approaches a constant value of approximately

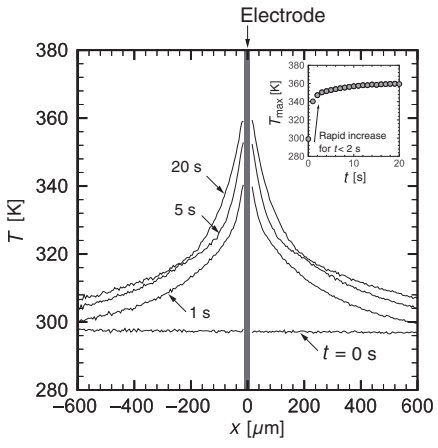

FIG. 2. Time development of the spatial profile of T. ΔH is set at 0 μm, and $\bar{U} \approx 0$ μm s^{-1}. (Inset) The time development of $T_{\max}$.

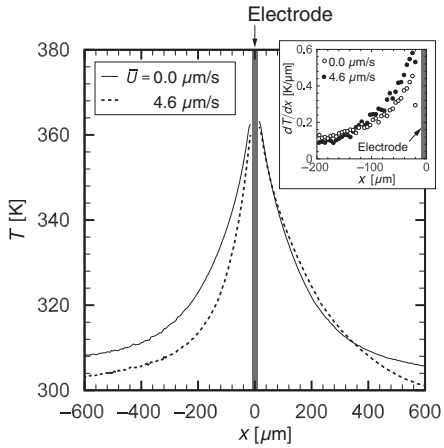

FIG. 3. Spatial profile of T at $t = 100$ s. The cases of $\bar{U} = 0.0$ and $\bar{U} = 4.6$ μm s^{-1} are shown. (Inset) The temperature gradient dT/dx for $x < 0$ μm.

360 K for $t > 2$ s. Therefore, we conclude that the temperature field near the electrode can be considered constant after 20 s.

Figure 3 shows the temperature profile at $t = 100$ s for the cases of $\Delta H = 0$ μm ($\bar{U} = 0.0$ μm s^{-1}) and $\Delta H = 100$ μm ($\bar{U} = 4.6$ μm s^{-1}) (see Table II). The inset shows the temperature gradient dT/dx near the electrode (-200 μm $< x < 0$ μm). The mean flow of $\bar{U} = 4.6$ μm s^{-1} in the x direction reduces the temperature T for $x < 0$ μm, which is attributable to the supply of the solution at room temperature. However, the inset shows that the temperature gradient is higher in the case of $\bar{U} = 4.6$ μm s^{-1} than that of $\bar{U} = 0.0$ μm s^{-1}. The temperature measurement results clarify that the microfluidic device developed in this paper can induce thermophoresis within a reasonable time scale of tens of seconds.

B. Thermophoresis of microparticles

The thermophoresis of the sample solutions is observed in cases 1–6 (see Table I). This section first addresses case 1, in which the PS beads are dispersed in the tris-HCl solution. Sequential snapshots of the observed florescence of the beads in case 1 near the center of the channel are shown in Fig. 4(a) at $t = 0$, 20, 40, 100, 200, and 300 s. The PS beads are observed to move away from the electrode. To qualitatively describe the behavior of the PS beads, the projection of the obtained images onto the x-t plane is shown in Fig. 4(b), which is produced by integrating the intensity of each snapshot in the y direction. Figure 4(b) also shows the trajectory of the peak intensity over time. The emergence of the peak intensity indicates an increased number density of the PS beads. Trajectories of the peaks indicate that the speed of the particles is approximately 1 μm s^{-1}. In this paper, the diameter of particles is 1 μm for all cases. From the Stokes-Einstein relation, we can estimate that the diffusion coefficient D

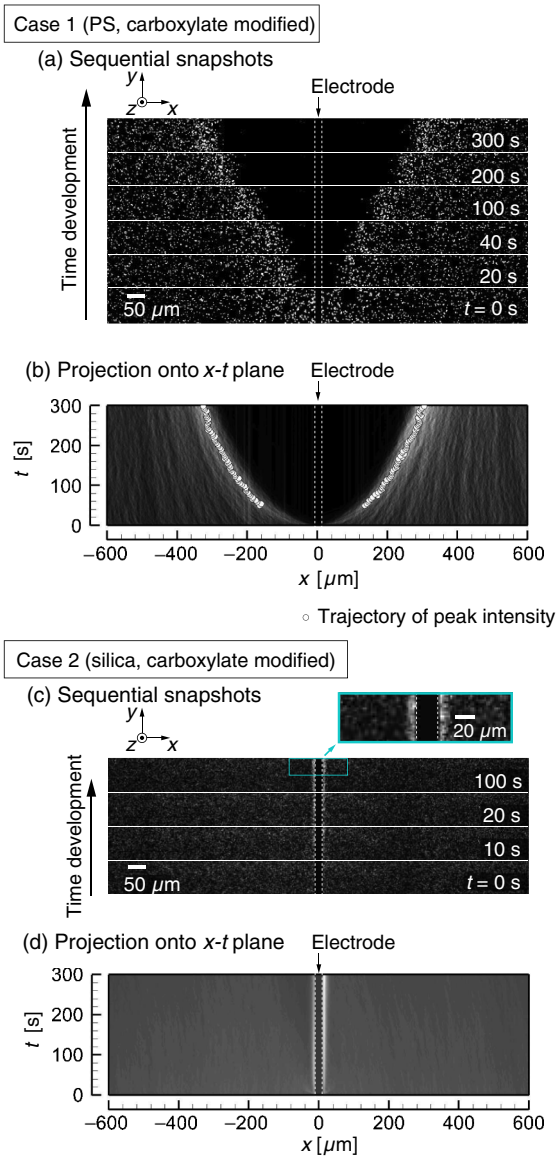

FIG. 4. (a) Sequential snapshots of fluorescent views in the microchannel at $t = 0$, 20, 40, 100, 200, and 300 s for case 1 (PS, carboxylate modified; see Table I). The edges of the thin-film electrode are indicated by dashed lines. (b) Projection of the snapshots onto the x-t plane for case 1. The intensity of the sequential snapshot (a) is integrated in the y direction and summarized in the x-t plane. The symbols represent the trajectory of the peak intensity over time. (c) Sequential snapshots of fluorescent views in the microchannel at $t = 0$, 10, 20, and 100 s for case 2 (silica, carboxylate modified; see Table I). (d) Projection of the snapshots onto the x-t plane for case 2. Comparisons between (a) and (c) and between (b) and (d) demonstrate the opposite responses of the PS and silica beads to the temperature gradient. Note that the surface modifications, diameters, and solvents in cases 1 and 2 are the same.

of the particle is 4×10^{-13} m^2 s^{-1} at room temperature. Therefore, the velocity of diffusion, which can be estimated using D/L_0, is $O(10^{-8})$ m s^{-1}, with the characteristic length $L_0 \approx 100$ μm. This speed is much slower than the observed velocity, and we conclude that the effect of diffusion is insignificant in our experiments.

Next, the results in case 1 are compared to those in case 2. In case 2, the silica beads are used instead of the PS beads, and the surfaces of both beads are carboxylate modified (Table I). The results for case 2 are shown in Figs. 4(c) and 4(d). The time development of the silica beads shown in Fig. 4(c) indicates that the beads reach the steady state at $t = 20$ s. In this case, the silica beads accumulate near the electrode. A comparison of Fig. 4(c) to Fig. 4(a) reveals that the silica and PS beads have the opposite response to the temperature gradient in the present microfluidic device despite the surface modifications, diameters, and solvents being the same. This opposite response indicates that the bulk characteristics may be affective on thermophoresis. Note that the thermal conductivity of the beads plays an important role in the theory of thermophoresis in both gases [49] and liquids [50]. Although the thermal conductivities $\lambda_{\mathrm{silica}}$ and λ_{PS} of the two beads are different, their orders are the same; therefore, we cannot attribute the opposite responses to the thermal conductivities. In fact, according to a theoretical model [26,50,51] based on slip flows along the surfaces of the beads, the magnitude of the differences between $\lambda_{\mathrm{PS}} \approx 0.15$ W m^{-1} K^{-1} and $\lambda_{\mathrm{water}} \approx 0.6$ W m^{-1} K^{-1} and between $\lambda_{\mathrm{silica}} \approx 1.3$ W m^{-1} K^{-1} and λ_{water} would cause the thermophoretic velocity of the PS beads to be twice that of the silica beads but would not produce the observed sign reversal. We also consider the difference in the surface charge of the particles since the electrolyte Seebeck effect has been known to change the sign of thermophoresis [24,25,37,52]. We measure the ζ potentials of particles using an electrophoretic light-scattering spectrophotometer (ELS-6000, Otsuka Electronics, Japan). The ζ potentials for cases 1 and 2 are -80 ± 3 and -79 ± 3 mV, respectively, and we conclude that the difference in surface charge is not the main reason for the sign change. In order to investigate the effect of electrolyte, we also carry out the experiments with a different electrolyte concentration 1-mM tris HCl. However, we do not observe any qualitative difference for either case 1 or case 2. The difference between the cases of 1 and 10-mM tris HCl is investigated quantitatively in Sec. III C for PS beads.

The results for case 3, in which silica beads without surface modification are used, are shown in Fig. 5(a). The tracking of the peak trajectory is noisy in the case of silica, because the silica beads produce a weaker fluorescence than the PS beads do. The results for case 3 shown in Fig. 5(a) indicate that the unmodified silica beads move toward the colder region in the microchannel. These results should be compared with those for the silica beads with surface modification shown in Fig. 4(d). Because the solutions are the same in Figs. 4(d) and 5(a), the significant difference between these two cases is whether the beads undergo surface modification.

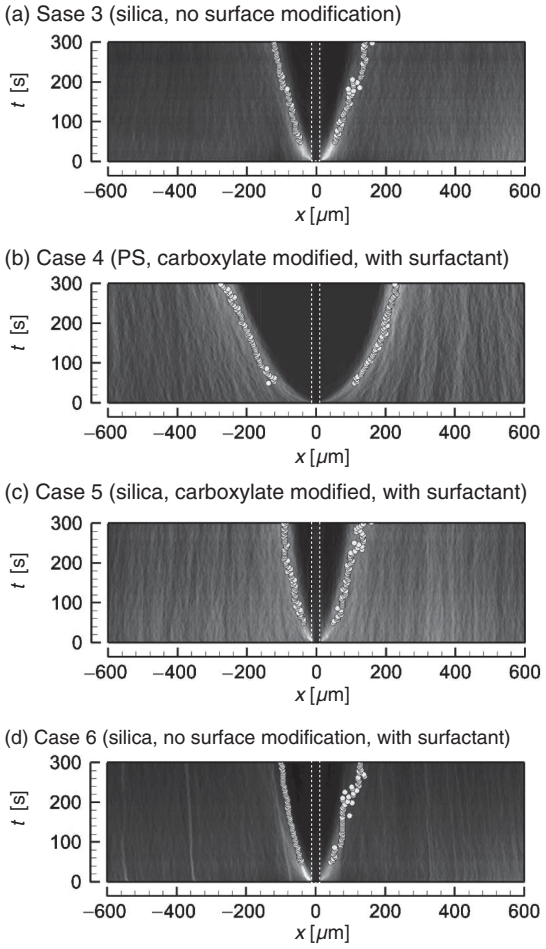

FIG. 5. Projection of the obtained snapshots on the x-t plane for (a) case 3, (b) case 4, (c) case 5, and (d) case 6. See also the captions of Fig. 4 and Table I. Comparing (a) to Fig. 4(d) reveals that the silica beads with and without carboxylate-modified surfaces have the opposite response. Comparing (b), (c), and (d) to Figs. 4(b), 4(d), and 5(a), respectively, shows the effect of the additive surfactant. For the case of the PS beads [Figs. 4(b) and 5(b)], the addition of surfactant reduces the thermophoretic motion. For the case of the carboxylate-modified silica beads [Figs. 4(d) and 5(c)], the addition of surfactant results in the opposite sign for the thermophoresis.

The effect of adding the nonionic surfactant to the solution is demonstrated in Figs. 5(b)–5(d). A comparison of Figs. 4(b) and 5(b) shows that the added surfactant reduces the thermophoresis of the PS beads. This reduction may be attributable to the decrease in the ζ potential of the PS beads resulting from the coating of these beads by surfactant molecules [26]. An interesting difference is observed in the comparison between the cases of carboxylate-modified silica without and with the added surfactant [Figs. 4(d) and 5(c), respectively]: in this case, the added surfactant results in the opposite response to the temperature gradient. Such a reversal in behavior caused by adding a surfactant was also reported in Ref. [23], where smaller PS beads with diameters of tens of nanometers are used. On the other hand, a comparison of Figs. 5(a) and 5(d) shows that the added surfactant barely influences the behavior of the unmodified silica beads. The similarity of the behaviors shown in Figs. 5(c) and 5(d) is the result of the standardization of the surface by a nonionic surfactant, as proposed in Ref. [23]; this similarity is evidence that surface modification has a significant influence on thermophoretic effects. From these experimental results, silica beads move toward colder regions if their surfaces are coated by the surfactant or if there is no surface modification. Therefore, the motion toward the electrode observed in Fig. 4(d) is the effect of carboxylate modification. Theoretical models [11,21,50] predict that thermophoretic mobility tends to be negative if the affinity of a beads' surface to the solvent is low. In the case of water or a water-based environment, this means that the beads' surfaces are hydrophobic. Because the silica beads used in this paper are composed of SiO_2 and are hydrophilic, the positive thermophoresis for unmodified, uncoated silica beads and silica beads coated with surfactant qualitatively agrees with theoretical predictions.

C. Evaluation of thermophoretic mobility

Before the thermophoretic mobility is assessed, the effect of thermal convection in the present device is estimated to ensure it is significantly less than the thermophoretic effect. To determine the effect of thermal convection, the fluid flow in the device is numerically simulated by solving the Navier-Stokes equations with the Boussinesq approximation. The boundary condition applied to the temperature field at the bottom is derived from experimental data obtained in the steady state, and the other boundaries are considered adiabatic. The flow speed is 0.045 μm s^{-1} near the electrode and decreases with increasing $|x|$; e.g., the speed is 0.01 μm s^{-1} at $|x| \approx 200$ μm. Therefore, the speeds of the beads obtained from the results shown in Figs. 4 and 5, which are on the order of 1 μm s^{-1}, are significantly greater than the flow speed produced by thermal convection. Thus, we conclude that the effect of thermal convection is negligible in the present microfluidic device.

Figure 6(a) shows the trajectories of peaks x_p in Figs. 4(b) and 5, and Fig. 6(b) shows the temperature profile for $t = 100$, 200, and 300 s. Here, we plot the average of the values for $x > 0$ and $x < 0$. These figures are used to evaluate D_T as follows. First, we obtain fitting curves to express the trajectories x_p and temperature T. We differentiate these fitting curves in Fig. 6(a) by t to calculate the thermophoretic velocity, v_T, and differentiate those in Fig. 6(b) by x to estimate the temperature gradient dT/dx. Then D_T is obtained by the relation (see, e.g., Ref. [25])

$$v_T = -D_T \left.\frac{dT}{dx}\right|_{x=x_p}, \tag{1}$$

where $t = 100$, 200, and 300 s are used. The thermophoretic mobility D_T and the corresponding temperature are

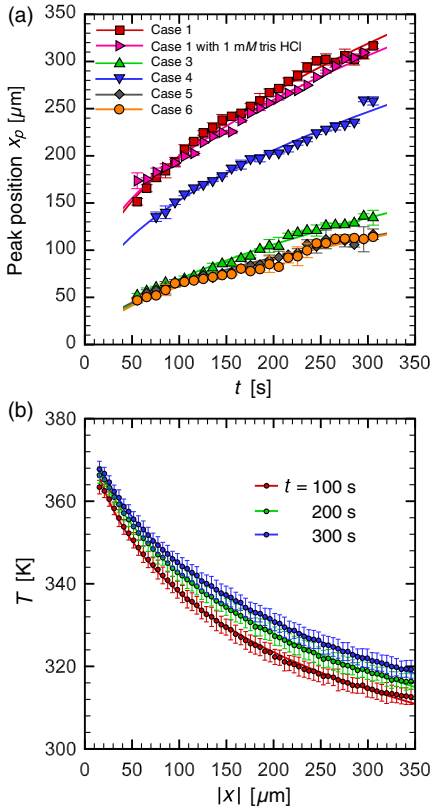

FIG. 6. (a) Trajectories of peak positions in Figs. 4 and 5. (b) Temperature profiles at $t = 100$, 200, and 300 s.

summarized in Table III. These values are the average of D_T at $t = 100$, 200, and 300 s. Case 1 results in the largest D_T value, as shown in Table III. The experiment of case 1 with a weaker-electrolyte, 1-mM tris-HCl solution, shows an 11% decrease in D_T. In our experiments, the concentration of tris HCl does not result in a drastic change of D_T.

For case 2 [Fig. 4(d)], the value of D_T appears to be negative because the silica beads accumulate near the electrode ($|x| < 20$ μm). Therefore, it is not possible to obtain D_T by the same procedure in this case. However, the range of accumulation is very small. More specifically, the silica beads at $|x| > 20$ μm cannot be attracted to the electrode within 300 s. This means that the thermophoretic velocity is, at most, $|v_T| < (20\ \mu\text{m})/(300\ \text{s}) \approx 0.07\ \mu\text{m s}^{-1}$, and thus $|D_T| < 0.2\ \mu\text{m}^2\ \text{s}^{-1}\ \text{K}^{-1}$. In this paper, only the silica beads with surface modification show negative thermophoresis. The $|D_T|$ value for this case is small relative to those in other cases of positive thermophoresis ($D_T > 1\ \mu\text{m}^2\ \text{s}^{-1}\ \text{K}^{-1}$).

TABLE III. Thermophoretic mobility D_T ($\mu\text{m}^2\ \text{s}^{-1}\ \text{K}^{-1}$) and temperature (K) for cases 1–6.

Case	D_T ($\mu\text{m}^2\ \text{s}^{-1}\ \text{K}^{-1}$)	T (K)
Case 1	6.85 ± 0.44	322 ± 1
Case 1 with 1-mM tris HCl	6.07 ± 0.46	322 ± 1
Case 2	$\lvert D_T \rvert < 0.2$	365 ± 1
Case 3	1.71 ± 0.01	341 ± 2
Case 4	4.30 ± 0.25	327 ± 1
Case 5	1.19 ± 0.03	344 ± 2
Case 6	1.20 ± 0.02	344 ± 2

The goal of this paper is to grasp the behaviors of the samples and demonstrate the potential use of thermophoresis in the microfluidic devices as separators of microparticles according to the differences in thermophoretic characteristics. Other methods of evaluating the thermophoretic mobility D_T of microparticles include thermal field-flow fractionation [24,35,37], beam deflection [1,2,23,36,52], and the use of a Soret cell [53–55] or a microgap Soret cell [25]. These techniques were used in past studies with the basic intent of quantifying thermophoresis rather than using it for a specific purpose in a fluidic device.

In summary, a comparison between the cases presented in Figs. 4 and 5 indicates that the PS beads are more sensitive to the temperature gradient than the silica beads and move toward the colder side of the device. Section III D focuses on the relatively large value of D_T in cases 1 and 4 to demonstrate dynamical pattern formation in a uniform flow. The remarkable difference between the D_T values for the PS and silica beads (cases 1 and 2) is also highlighted by demonstrating separation in the microfluidic device.

D. Pattern formation and separation

Pattern formation is demonstrated by using the solutions in cases 1 and 4. In the experiments described in Sec. III B, ΔH is set to zero. Here, ΔH is set to 100 μm, which induces a mean flow of $\bar{U} \approx 4.6\ \mu\text{m s}^{-1}$. The results for case 1 are summarized in Fig. 7. Figure 7(a) shows the sequential snapshots for $t = 0$, 50, 100, and 150 s, with the flow induced in the positive x direction (rightward). The PS beads are observed to accumulate near the left side of the electrode. No PS beads pass through the electrode, and thus the beads in the region of $x > 0$ μm are flushed away over time. Figure 7(b) shows the x-t projection of the images with the intensity displayed on a logarithmic scale. Note that the intensity can be directly converted to the number density of the PS beads. The diagonal dashed line, which serves as a guide for the eye, indicates a mean flow of $\bar{U} \approx 4.6\ \mu\text{m s}^{-1}$. An increase in the concentration of the PS beads is observed at $x \approx -65$ μm. Figure 7(c) shows the spatial profiles of the relative intensity P for $t = 0$, 50, 100, 150, 200, 250, and 300 s. The concentration of the PS beads is found to be nearly 100 times higher than that at the initial time. Figure 7(d) shows $P_{\max} = \max_x(P)$ as a function of time, and $P_{\max}$ is found to linearly increase with time. The linear increase is due to the fact that the particles are supplied to the concentrated position (i.e., $x \approx -65$ μm) at a constant rate. Note that the volume fraction of particles in this experiment now increases up to 4%. However, we do

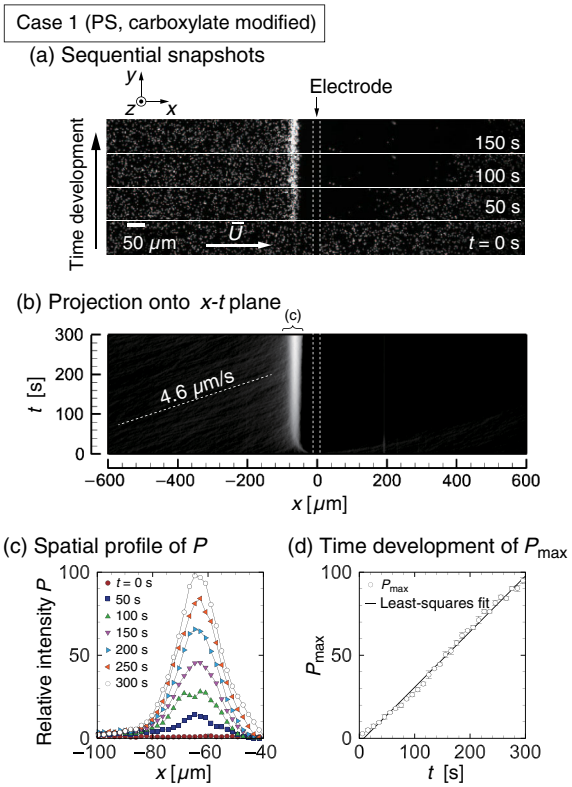

FIG. 7. (a) Sequential snapshots of fluorescent views in the microchannel at $t = 0$, 50, 100, and 150 s for case 1 with $\bar{U} = 4.6\ \mu\mathrm{m\,s^{-1}}$. (b) Projection of the snapshots onto the x-t plane, where the intensity is shown on a logarithmic scale. The dashed line at $\bar{U} = 4.6\ \mu\mathrm{m\,s^{-1}}$ serves as a guide for the eye. See also the caption of Fig. 4. (c) Spatial profile of the intensity P near the electrode. (d) Time development of $P_{\max} = \max_x(P)$.

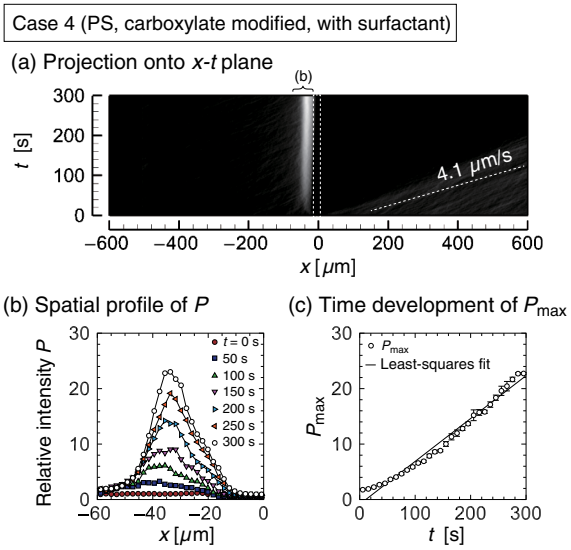

FIG. 8. (a) Projection of snapshots onto the x-t plane for case 4 with the intensity is shown on a logarithmic scale. The dashed line at $4.1\ \mu\mathrm{m\,s^{-1}}$ serves as a guide for the eye. See also the caption of Fig. 4. (b) Spatial profile of the intensity P near the electrode. (c) Time development of $P_{\max} = \max_x(P)$.

not observe the finite-size effect of particles for the experimental time presented in this paper.

The results of the same trial for case 4 are shown in Fig. 8; the difference between cases 1 and 4 is that the surfactant is added to the solution in case 4. The projection in Fig. 8(a) shows that the PS beads are transported downstream by the mean flow $\bar{U}$. However, the concentration of PS beads at the electrode is high, as in case 1. The spatial profile of the intensity P is shown in Fig. 8(b). These results show that the intensity increases over time and that the maximum concentration is 24 times higher than the initial concentration. The position of the greatest concentration increase is $x \approx -35\ \mu$m, which is different from that in case 1. The time development of $P_{\max}$ shows linear growth, as shown in Fig. 8(c). Figures 7 and 8 show that the thermophoresis induced by the Joule heating of the thin-film line electrode embedded in the microfluidic channel leads to the pattern formation. By parallelizing the channel, the thermophoresis may work as a selective microparticle filter that can be used to detect dilute analytes (e.g., cells or biomolecules) in a sample solution.

D_T can be roughly estimated from these experiments as follows. The PS beads accumulate most at $x \approx -65\ \mu$m for case 1 [Fig. 7(c)], where the mean velocity v_{bead} of the PS beads may be regarded as $v_{\mathrm{bead}} \approx 0\ \mu\mathrm{m\,s^{-1}}$ and the temperature gradient $dT/dx \approx 0.4\ \mathrm{K\,\mu m^{-1}}$, as shown in the inset of Fig. 3. Therefore, under the supposition that $v_{\mathrm{bead}} \approx \bar{U} + v_T$, Eq. (1) yields $D_T = \bar{U}/(dT/dx) \approx 11.5\ \mu\mathrm{m^2\,s^{-1}\,K^{-1}}$, where we take the temperature to be $T \approx 337$ K from Fig. 3. The same estimate can be made for case 4 [Fig. 8(b)]. In this case, the PS beads accumulate at $x \approx -35\ \mu$m, where the temperature gradient is $dT/dx \approx 0.5\ \mathrm{K\,\mu m^{-1}}$, as shown in the inset of Fig. 3. Considering that $\bar{U} \approx 4.1\ \mu\mathrm{m\,s^{-1}}$ yields $D_T \approx 8.2\ \mu\mathrm{m^2\,s^{-1}\,K^{-1}}$, where we take the temperature to be $T \approx 349$ K from Fig. 3. Since D_T tends to grow as temperature increases [22], these values are greater than those displayed in Table III.

Finally, the separation of the mixed solution is demonstrated. The PS and silica beads with a carboxylate surface modification (cases 1 and 2) are mixed because they are expected to have opposite responses to the temperature gradient (Fig. 4). The mean flow is set at $\bar{U} = 4.6\ \mu\mathrm{m\,s^{-1}}$. Sequential snapshots for this experiment are shown in Fig. 9. For $t < 300$ s, a mirror unit (U-FGW, Olympus, Japan) is used to observe both beads. Figure 9 shows that some beads accumulate near the left side of the electrode, and some are transported to the downstream region. To identify the PS beads, the mirror unit is changed to a different unit (U-FBW, Olympus, Japan) at $t = 300$ s, which allow the observation of only the PS beads. The PS beads are observed to be trapped in the upstream region, as in Fig. 5(a). Therefore, we conclude that the downstream beads, which are observed for $t < 300$ s and $x > 0\ \mu$m, are the silica beads. This is a clear demonstration that it is

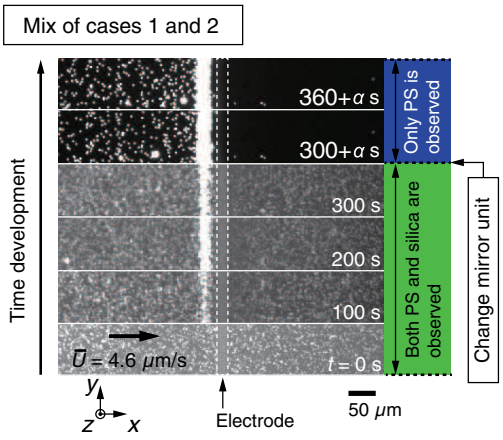

FIG. 9. Sequential snapshots of fluorescent views in the microchannel for the mixed solution of the PS and silica beads with a carboxylate surface modification. The mean flow is set to $\bar{U} = 4.6\ \mu\mathrm{m\,s^{-1}}$. For the time range $0\ \mathrm{s} < t < 300\ \mathrm{s}$, both beads are observable. At the time $t = 300$ s, the mirror unit is changed to a unit with different optical characteristics such that only the PS beads could be observed for $t > 300$ s.

possible to separate beads composed of different materials with the same diameters and surface modifications using thermophoresis in a microfluidic channel.

IV. CONCLUDING REMARKS

This paper proposes the use of the thermophoresis of microparticles for pattern formation and separation in an on-chip microfluidic device. Thermophoresis is induced by the Joule heating of a thin-film electrode fabricated using MEMS technologies.

First, the thermophoresis of PS and silica beads is investigated. It is found that PS beads with a carboxylate surface modification moves toward the colder region in the device, whereas silica beads with the same surface modification show the opposite response to the temperature gradient. The difference between thermophoretic responses originating from differences in the material may lead to the development of a microfluidic separation technique for target objects with the same size and surface conditions (or surface charges). Such objects may otherwise be difficult to separate using only hydrodynamic [56] or electrophoretic [57] separation. The thermophoretic separation of the PS and silica beads is demonstrated clearly in the last part of this paper.

The silica beads with and without the carboxylate surface modification also show the opposite response to the temperature gradient; that is, the silica beads with and without surface modification move toward the hotter and colder sides of the device, respectively. Differences in the thermophoretic response originating from the surface conditions are particularly important in the application of the proposed technique to biomedical devices because the surface conditions affect the agglomeration state, which is related to the toxicity potential [58]. However, the addition of a nonionic surfactant to the silica beads with and without surface modification causes them to show the same thermophobic behavior. Therefore, the use of a surfactant may result in poor thermophoretic separation.

The interplay between the thermophoresis and the mean flow in the microchannel is found to result in the localized concentration of the PS beads in the upstream region. A purified solution is obtained at the downstream region; that is, filtration of the PS beads is demonstrated. Such a filtration technique and the abovementioned separation concept based on thermophoresis can be easily integrated into the existing microfluidic devices and will therefore expand the potential of nano- and microfluidic devices by adding an alternative control principle.

ACKNOWLEDGMENTS

This work was supported by JSPS KAKENHI Grant No. JP15K17973 for Young Scientists (B) and JSPS KAKENHI Grant No. JP16H06504 in Scientific Research on Innovative Areas "Nano-Material Optical-Manipulation".

APPENDIX: FABRICATION OF THE MICROFLUIDIC DEVICE

The glass substrate is cleaned with dimethylformamide, ethanol, and deionized water in series. After the substrate is dried, it is spin coated with a positive photoresist (AZ 5214 E, Merck, Germany). Lithographic exposure is applied to the substrate using a photomask with the pattern of the electrode, and the exposed part of the photoresist is removed by a developer (AZ 300 MIF, Merck, Germany). As a result, the substrate with the patterned layer of the photoresist is obtained. Then Cr and Au are deposited on the substrate in series, where the thickness of the Cr and Au thin films are 5 and 150 nm, respectively. Finally, the substrate is immersed in acetone to remove the remaining photoresist.

The PDMS block with the microchannel is also fabricated by photolithography. A negative photoresist (SU-8 3025, MicroChem, Westborough, Massachusetts) is spin coated onto a silicon substrate. After the lithographic exposure is applied to the substrate using a photomask with the pattern of the microchannel, the unexposed part of the photoresist is removed by a developer (SU-8 developer, MicroChem, Westborough, Massachusetts). A 10:1 mixture of uncured PDMS and curing agent is poured in a chamber containing the substrate with the SU-8 pattern to the bottom. The PDMS is cured by heating the chamber, after which it is ready for use in the microfluidic device.

[1] R. Piazza, Thermophoresis: Moving particles with thermal gradients, Soft Matter **4**, 1740 (2008).
[2] R. Piazza and A. Parola, Thermophoresis in colloidal suspensions, J. Phys. Condens. Matter **20**, 153102 (2008).

[3] A. Würger, Thermal non-equilibrium transport in colloids, Rep. Prog. Phys. **73**, 126601 (2010).
[4] A. Würger, Thermophoresis in Colloidal Suspensions Driven by Marangoni Forces, Phys. Rev. Lett. **98**, 138301 (2007).
[5] A. Würger, Transport in Charged Colloids Driven by Thermoelectricity, Phys. Rev. Lett. **101**, 108302 (2008).
[6] A. Würger, Molecular-Weight Dependent Thermal Diffusion in Dilute Polymer Solutions, Phys. Rev. Lett. **102**, 078302 (2009).
[7] T. Tsuji, S. Saita, and S. Kawano, Thermophoresis of a Brownian particle driven by inhomogeneous thermal fluctuation, Physica (Amsterdam) **493A**, 467 (2018).
[8] G. Galliéro and S. Volz, Thermodiffusion in model nanofluids by molecular dynamics simulations, J. Chem. Phys. **128**, 064505 (2008).
[9] D. Lüsebrink, M. Yang, and M. Ripoll, Thermophoresis of colloids by mesoscale simulations, J. Phys. Condens. Matter **24**, 284132 (2012).
[10] T. Tsuji, H. Iseki, I. Hanasaki, and S. Kawano, Molecular dynamics study of force acting on a model nano particle immersed in fluid with temperature gradient: Effect of interaction potential, AIP Conf. Proc. **1786**, 110003 (2016).
[11] T. Tsuji, H. Iseki, I. Hanasaki, and S. Kawano, Negative thermophoresis of nanoparticles interacting with fluids through a purely-repulsive potential, J. Phys. Condens. Matter **29**, 475101 (2017).
[12] L. Lin, J. Zhang, X. Peng, Z. Wu, A. C. H. Coughlan, Z. Mao, M. A. Bevan, and Y. Zheng, Opto-thermophoretic assembly of colloidal matter, Sci. Adv. **3**, e1700458 (2017).
[13] S. Duhr and D. Braun, Optothermal Molecule Trapping by Opposing Fluid Flow with Thermophoretic Drift, Phys. Rev. Lett. **97**, 038103 (2006).
[14] C. J. Wienken, P. Baaske, U. Rothbauer, D. Braun, and S. Duhr, Protein-binding assays in biological liquids using microscale thermophoresis, Nat. Commun. **1**, 100 (2010).
[15] S. A. Seidel, C. J. Wienken, S. Geissler, M. Jerabek-Willemsen, S. Duhr, A. Reiter, D. Trauner, D. Braun, and P. Baaske, Label-free microscale thermophoresis discriminates sites and affinity of protein–ligand binding, Angew. Chem., Int. Ed. Engl. **51**, 10656 (2012).
[16] J. L. Parker and S. Newstead, Molecular basis of nitrate uptake by the plant nitrate transporter NRT1.1, Nature (London) **507**, 68 (2014).
[17] Y. T. Maeda, A. Buguin, and A. Libchaber, Thermal Separation: Interplay between the Soret Effect and Entropic Force Gradient, Phys. Rev. Lett. **107**, 038301 (2011).
[18] Y. T. Maeda, T. Tlusty, and A. Libchaber, Effects of long DNA folding and small RNA stem-loop in thermophoresis, Proc. Natl. Acad. Sci. U.S.A. **109**, 17972 (2012).
[19] S. Duhr and D. Braun, Why molecules move along a temperature gradient, Proc. Natl. Acad. Sci. U.S.A. **103**, 19678 (2006).
[20] P. Reineck, C. J. Wienken, and D. Braun, Thermophoresis of single stranded DNA, Electrophoresis **31**, 279 (2010).
[21] S. A. Putnam and D. G. Cahill, Transport of nanoscale latex spheres in a temperature gradient, Langmuir **21**, 5317 (2005).
[22] S. Iacopini, R. Rusconi, and R. Piazza, The "macromolecular tourist": Universal temperature dependence of thermal diffusion in aqueous colloidal suspensions, Eur. Phys. J. E **19**, 59 (2006).
[23] M. Braibanti, D. Vigolo, and R. Piazza, Does Thermophoretic Mobility Depend on Particle Size?, Phys. Rev. Lett. **100**, 108303 (2008).
[24] D. Vigolo, R. Rusconi, H. A. Stone, and R. Piazza, Thermophoresis: Microfluidics characterization and separation, Soft Matter **6**, 3489 (2010).
[25] T. Tsuji, K. Kozai, H. Ishino, and S. Kawano, Direct observations of thermophoresis in microfluidic systems, Micro Nano Lett. **12**, 520 (2017).
[26] L. Lin, X. Peng, Z. Mao, X. Wei, C. Xie, and Y. Zheng, Interfacial-entropy-driven thermophoretic tweezers, Lab Chip **17**, 3061 (2017).
[27] L. Lin, X. Peng, X. Wei, Z. Mao, C. Xie, and Y. Zheng, Thermophoretic tweezers for low-power and versatile manipulation of biological cells, ACS Nano **11**, 3147 (2017).
[28] J. Burelbach, M. Zupkauskas, R. Lamboll, Y. Lan, and E. Eiser, Colloidal motion under the action of a thermophoretic force, J. Chem. Phys. **147**, 094906 (2017).
[29] J. Chen, H. Cong, F.-C. Loo, Z. Kang, M. Tang, H. Zhang, S.-Y. Wu, S.-K. Kong, and H.-P. Ho, Thermal gradient induced tweezers for the manipulation of particles and cells, Sci. Rep. **6**, 35814 (2016).
[30] Y. He, M. Tsutsui, R. H. Scheicher, F. Bai, M. Taniguchi, and T. Kawai, Thermophoretic manipulation of DNA translocation through nanopores, ACS Nano **7**, 538 (2013).
[31] M. Tsutsui, M. Taniguchi, K. Yokota, and T. Kawai, Identifying single nucleotides by tunnelling current, Nat. Nanotechnol. **5**, 286 (2010).
[32] C. Kawaguchi, T. Noda, M. Tsutsui, M. Taniguchi, S. Kawano, and T. Kawai, Electrical detection of single pollen allergen particles using electrode-embedded microchannels, J. Phys. Condens. Matter **24**, 164202 (2012).
[33] M. Tsutsui, Y. Maeda, Y. He, S. Hongo, S. Ryuzaki, S. Kawano, T. Kawai, and M. Taniguchi, Trapping and identifying single-nanoparticles using a low-aspect-ratio nanopore, Appl. Phys. Lett. **103**, 013108 (2013).
[34] S. Tanaka, M. Tsutsui, H. Theodore, H. Yuhui, A. Arima, T. Tsuji, K. Doi, S. Kawano, M. Taniguchi, and T. Kawai, Tailoring particle translocation via dielectrophoresis in pore channels, Sci. Rep. **6**, 31670 (2016).
[35] A. Regazzetti, M. Hoyos, and M. Martin, Experimental evidence of thermophoresis of non-Brownian particles in pure liquids and estimation of their thermophoretic mobility, J. Phys. Chem. B **108**, 15285 (2004).
[36] R. Piazza, Thermal diffusion in ionic micellar solutions, Philos. Mag. **83**, 2067 (2003).
[37] K. A. Eslahian, A. Majee, M. Maskos, and A. Würger, Specific salt effects on thermophoresis of charged colloids, Soft Matter **10**, 1931 (2014).
[38] D. Braun and A. Libchaber, Trapping of DNA by Thermophoretic Depletion and Convection, Phys. Rev. Lett. **89**, 188103 (2002).
[39] H.-R. Jiang, H. Wada, N. Yoshinaga, and M. Sano, Manipulation of Colloids by a Nonequilibrium Depletion Force in a Temperature Gradient, Phys. Rev. Lett. **102**, 208301 (2009).

[40] R. T. Schermer, C. C. Olson, J. P. Coleman, and F. Bucholtz, Laser-induced thermophoresis of individual particles in a viscous liquid, Opt. Express **19**, 10571 (2011).
[41] A. I. K. Lao, T. M. H. Lee, I-M. Hsing, and N. Y. Ip, Precise temperature control of microfluidic chamber for gas and liquid phase reactions, Sens. Actuators A **84**, 11 (2000).
[42] G. V. Kaigala, V. N. Hoang, A. Stickel, J. Lauzon, D. Manage, L. M. Pilarski, and C. J. Backhouse, An inexpensive and portable microchip-based platform for integrated RTPCR and capillary electrophoresis, Analyst **133**, 331 (2008).
[43] D. Vigolo, R. Rusconi, R. Piazza, and H. A. Stone, A portable device for temperature control along microchannels, Lab Chip **10**, 795 (2010).
[44] M. Furuhashi, Y. Okamoto, D. Onoshima, T. Ohshiro, S. Ryuzaki, K. Yokota, M. Tsutsui, M. Taniguchi, K. Nakatani, Y. Baba, and T. Kawai, High speed DNA denaturation using microheating devices, Appl. Phys. Lett. **103**, 023112 (2013).
[45] R. P. Sheldon, *Composite Polymeric Materials* (Elsevier Science, New York, 1982).
[46] S. Yu, P. Hing, and X. Hu, Thermal conductivity of polystyrene–aluminum nitride composite, Composites Part A **33**, 289 (2002).
[47] P. Jund and R. Jullien, Molecular-dynamics calculation of the thermal conductivity of vitreous silica, Phys. Rev. B **59**, 13707 (1999).
[48] H. Bruus, *Theoretical Microfluidics* (Oxford University Press, Oxford, 2007).
[49] Y. Sone, *Molecular Gas Dynamics: Theory, Techniques, and Applications* (Birkhäuser Boston, Cambridge, MA, 2007).
[50] J. L. Anderson, Colloid transport by interfacial forces, Annu. Rev. Fluid Mech. **21**, 61 (1989).
[51] S. A. Putnam, D. G. Cahill, and G. C. L. Wong, Temperature dependence of thermodiffusion in aqueous suspensions of charged nanoparticles, Langmuir **23**, 9221 (2007).
[52] D. Vigolo, S. Buzzaccaro, and R. Piazza, Thermophoresis and thermoelectricity in surfactant solutions, Langmuir **26**, 7792 (2010).
[53] G. S. McNab and A. Meisen, Thermophoresis in liquids, J. Colloid Interface Sci. **44**, 339 (1973).
[54] P. Kolodner, H. Williams, and C. Moe, Optical measurement of the Soret coefficient of ethanol/water solutions, J. Chem. Phys. **88**, 6512 (1988).
[55] A. Mialdun and V. Shevtsova, Temperature dependence of Soret and diffusion coefficients for toluene–cyclohexane mixture measured in convection-free environment, J. Chem. Phys. **143**, 224902 (2015).
[56] M. Yamada and M. Seki, Hydrodynamic filtration for on-chip particle concentration and classification utilizing microfluidics, Lab Chip **5**, 1233 (2005).
[57] U. Pyell, Characterization of nanoparticles by capillary electromigration separation techniques, Electrophoresis **31**, 814 (2010).
[58] J. Jiang, G. Oberdörster, and P. Biswas, Characterization of size, surface charge, and agglomeration state of nanoparticle dispersions for toxicological studies, J. Nanopart. Res. **11**, 77 (2009).